Surface Science 605 (2011) 582–592

Contents lists available at ScienceDirect

Surface Science

journal homepage: www.elsevier.com/ locate/susc

First-principles investigations of $Ni_3Al(111)$ and NiAl(110) surfaces at metal dusting conditions

Souheil Saadi [a,b], Berit Hinnemann [b,*], Charlotte C. Appel [b], Stig Helveg [b], Frank Abild-Pedersen [a,c], Jens K. Nørskov [a,c,d]

[a] Center for Atomic-scale Materials Design, Department of Physics, Technical University of Denmark, DK-2800 Kgs. Lyngby, Denmark
[b] Haldor Topsøe A/S, Nymøllevej 55, DK-2800 Kgs. Lyngby, Denmark
[c] Center for Interface Science and Catalysis, SLAC National Accelerator Laboratory, 2575 Sand Hill Road, Menlo Park, CA 94025, USA
[d] Department of Chemical Engineering, Stanford University, Stanford, CA 94305, USA

ARTICLE INFO

Article history:
Received 9 November 2010
Accepted 21 December 2010
Available online 28 December 2010

Keywords:
Metal dusting
Oxide scale
Steam reforming
Ni alloys
Density functional theory
Ni_3Al
NiAl
Carbon

ABSTRACT

We investigate the structure and surface composition of the γ′-$Ni_3Al(111)$ and β-NiAl(110) alloy surfaces at conditions relevant for metal dusting corrosion related to catalytic steam reforming of natural gas. In regular service as protective coatings, nickel–aluminum alloys are protected by an oxide scale, but in case of oxide scale spallation, the alloy surface may be directly exposed to the reactive gas environment and vulnerable to metal dusting. By means of density functional theory and thermochemical calculations for both the Ni_3Al and NiAl surfaces, the conditions under which CO and OH adsorption is to be expected and under which it is inhibited, are mapped out. Because CO and OH are regarded as precursors for nucleating graphite or oxide on the surfaces, phase diagrams for the surfaces provide a simple description of their stability. Specifically, this study shows how the CO and OH coverages depend on the steam to carbon ratio (S/C) in the gas and thereby provide a ranking of the carbon limits on the different surface phases.

© 2010 Elsevier B.V. All rights reserved.

1. Introduction

In catalytic steam reforming, natural gas is reacted with steam to form synthesis gas or hydrogen. The constant pursuit for maximum energy efficiency in modern steam reforming plants yields both economical and environmental benefits. For a steam reforming plant to operate at maximum efficiency and deliver a high throughput of desired product composition, it is essential to keep the S/C ratio low. Operation at low S/C is often accompanied by challenges in the development of materials [1]. The present work deals with a high-temperature corrosion phenomena known as metal dusting, which occurs in steam reforming plants operating at a low steam to carbon ratio (S/C) [1–3]. Metal dusting is a catastrophic form of carburisation, which attacks metal hardware, often consisting of Ni alloys. The metal is supersaturated with carbon, which forms graphite by inwards growth into the metal, and which finally breaks up the metal into particles and graphite [2,3]. Similar challenges may also occur in solid oxide fuel cells [4,5]. Metal dusting can occur at carbon activities greater than unity $a_C > 1$ and in the temperature interval of 350–800°.

Several studies [6–8] have shown that metal dusting is related to metal-catalysed graphite growth. The dissociative adsorption of carbon precursors on a Ni(-alloy) surface leads to the first graphene nucleation, subsequent graphite growth and finally metal dusting. Recent in-situ high-resolution transmission electron microscopy [9] and density functional theory (DFT) [10] studies have shown that steps on the metal surface act as growth centers for graphene. The modification of these growth centers is of great importance to avoid graphene nucleation. A recent study showed that the kinetics of graphene nucleation may be decreased by increasing the epitaxial mismatch between the metal and graphene basal plane [11]. This can be done by the addition of alloying elements as for instance Cu [4,12,13], Sn [14–16] or Au [17,18]. These are alloying elements well-known to inhibit metal dusting. Sn, Cu and Au also protect Ni surfaces by being less reactive towards carbon, and decrease the carbon solubility in the alloy. Selective poisoning of graphite growth centers on the surface is another option and can be done by adding sulphur or alkali metals in the feed gas [1,2]. A disadvantage of gas additives in steam reforming plants is the need for continuous feed and subsequent cleaning of the process gas. A different strategy is to alloy Ni with metals that may form protective oxide coatings, for instance Ti or Al [19–24].

Here, we focus on Al as an oxidative alloying element for stabilising Ni surfaces against metal dusting corrosion. As pointed out by Young [23] there are only few studies of the metallic Ni–Al

* Corresponding author. Tel.: +45 4527 2130; fax: +45 4527 2999.
E-mail address: behi@topsoe.dk (B. Hinnemann).

0039-6028/$ – see front matter © 2010 Elsevier B.V. All rights reserved.
doi:10.1016/j.susc.2010.12.023

alloys [20,22,25,26] in a metal dusting environment. The Fe_3Al and Ni_3Al alloys have been investigated by Grabke and co-workers [20] in short term metal dusting experiments followed by characterisation. It was concluded that Fe_3Al is susceptible to metal dusting while Ni_3Al showed excellent resistance. Later, Liu and Chen [22,27] investigated Ni_3Al in metal dusting experiments with exposures up to 500 h followed by characterisation. They concluded that pre-oxidation of Ni_3Al and thus formation of a thin Al_2O_3 layer improved the resistance towards carbon attack. The adhesion of α-$Al_2O_3(0001)/\beta$-NiAl was investigated by DFT in a study by Carling and Carter [28]. They found that Hf increases the work of adhesion between the metal-oxide interface, whereas elements such as S decrease it. This shows that the oxide may fall off during operation, which is also reported in experiments [23,29]. β-NiAl is also used as bi-metallic catalyst [30], and the present study therefore also may have relevance to the field of catalysis. The surface stoichiometry of β-NiAl in the early stages of oxidation was investigated by DFT calculations by Lozovoi et al. [31] and the structure of the ultra thin aluminum oxide film on NiAl(110) was reported by Kresse et al. [32], who combined scanning tunneling microscopy and DFT. They found the stoichiometry and geometry of the aluminum oxide film to be different from the bulk oxide. Under operating conditions in a metal dusting environment, the surface of the Ni–Al alloys is expected to be covered with an oxide scale, but as already discussed, this oxide scale can be damaged easily. In this case, the metal surface is directly exposed to the gas and is vulnerable to metal dusting.

Application of an aluminide coating on a Ni alloy leads to interdiffusion between the coating and the alloy at the high operation temperatures in a reforming plant. This will result in the existence of various Ni–aluminide phases in the coating [24]. In this work, we focus on the case of oxide failure on the γ'-Ni_3Al and β-NiAl surfaces and investigate, which adsorbates are present on the metallic surfaces under metal dusting conditions. For the close-packed γ'-$Ni_3Al(111)$ and β-NiAl(110) surfaces, phase diagrams are established, which show whether the surface is covered by oxidation or carburisation precursors, modeled by the adsorption of OH and CO, respectively. Possible changes in the alloy surface stoichiometry induced by the presence of the adsorbates are taken into account. In this way, we study the interplay between the gas-composition and the surface composition. The results are extended to relevant conditions by the previously used chemical potential formalism [16,33,34]. In this way, we can gain insight into which conditions may cause carburisation or favor oxidation of the surfaces.

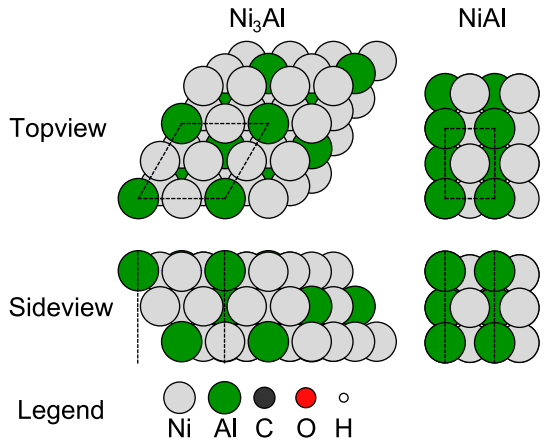

Fig. 1. Models for the $Ni_3Al(111)$ and the NiAl(110) surfaces. The surfaces are modeled by an in-plane (2×2) unit cell for the $Ni_3Al(111)$ surface and (1×1) unit cell for the NiAl(110) surface and three layers in the z-direction. Color code: light gray (Ni), green (Al), charcoal black (C), red (O), and white (H). The same color code is used in all subsequent ball-models.

Table 1
The chemical potential of the gas phase species at standard conditions.

μ_X^0[eV]	C (s)	CO	H_2O (g)	H_2
	−0.01	−0.52	−0.48	−0.32

2. Computational details

2.1. Computational methods

All DFT calculations are carried out using the plane-wave pseudopotential code Dacapo [35] within the Atomic Simulation Environment framework [36,37]. The Kohn–Sham wave functions are expanded in a plane-wave basis set, with a kinetic energy up to 400 eV for bulk calculations and 350 eV for surfaces and molecules. The cut-off energy for the density grid [38] is set to 800 eV for bulk calculations and 700 eV for calculations including surfaces and molecules. All core electrons of the ions are described by ultrasoft pseudopotentials [38–40], and the exchange and correlation effects are described using the revised Perdew–Ernzerhoff–Burke (RPBE) functional [41]. The k-point sampling of the first Brillouin zone is performed with a $(8\times8\times8)$ Monkhorst–Pack grid [42] for all bulk calculations, a $(8\times8\times1)$ grid for $Ni_3Al(111)$ surfaces, a $(12\times12\times1)$ for NiAl(110) surfaces and a $(1\times1\times1)$ grid for molecules. The self-consistent electron density is determined by iterative diagonalisation of the Kohn–Sham Hamiltonian, and the resulting Kohn–Sham eigenstates are populated following a Fermi distribution ($k_BT=0.1$ eV). Pulay mixing [43] of the resulting electronic density is used and the resulting total energy extrapolated to zero temperature. All results on pure Ni(111) are taken from reference [11]. The calculations on pure Ni(111) were performed spin-polarised. The calculations on Ni_3Al and NiAl were initially performed spin-polarised for the clean alloy surface, but no magnetic moments were found. Therefore, all subsequent calculations were performed without spin polarisation.

In all bulk calculations, the structure is optimised by allowing the atoms, as well as the unit cell, to relax. The unit cell stresses are relaxed until all stress components are lower than 0.1 GPa. For the surface calculations, the bottom layer atoms are kept fixed in the calculated bulk positions while the top two layers and the adsorbate atoms are allowed to relax. For the calculations on molecules in the gas phase, all atoms are allowed to relax. The structure optimisations are all performed with the Quasi–Newton (QN) algorithm, until the maximum force on any ion is less than 0.03 eV/Å. The periodic slabs are separated by 10 Å of vacuum; and a correction for the surface dipole interaction is applied [44]. In order to obtain thermochemical quantities, vibrational calculations are performed. In a harmonic potential approximation, the energy change is calculated as the relevant atom is displaced in the $\pm$x, $\pm$y and $\pm$z directions with a displacement length of around 1% of the relevant bond length. This value of the displacement has to be set low in order not to violate the harmonic potential approximation, although not lower than the density-functional theory accuracy. The applied value is 0.03 Å in all cases. In all ball-models, we use colors for the different chemical species according to the legend in Fig. 1.

Table 2
Carbon activities and chemical potentials at the conditions applied by Rosado and Schütze [19] relative to the chemical potentials in standard state and conditions. Water is relative to water in the gas-phase at standard conditions.

T [°C]	T [K]	a_C	$\Delta\mu$ (C) [eV]	$\Delta\mu$ (CO) [eV]	$\Delta\mu$ (H_2O) [eV]	$\Delta\mu$ (H_2) [eV]
400	673.15	9904	0.54	−0.90	−0.88	−0.64
620	893.15	25.63	0.26	−1.45	−1.41	−1.03
700	973.15	5.58	0.16	−1.65	−1.61	−1.17

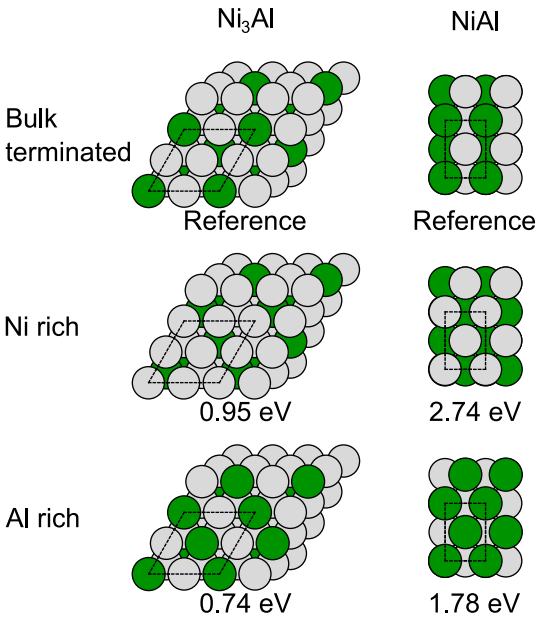

Fig. 2. Top-views of bulk, Ni-rich and Al-rich terminations of $Ni_3Al(111)$ and NiAl(110). All energies are per unit cell and referenced to the bulk termination. The overall stoichiometry within the unit cell is preserved in all cases.

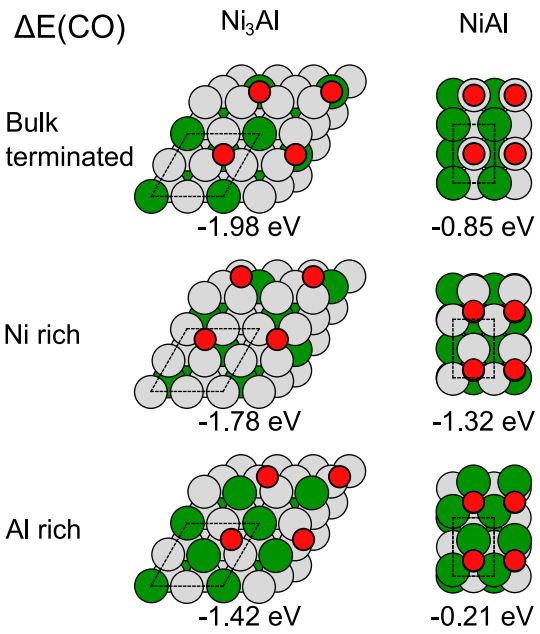

Fig. 3. CO adsorption on $Ni_3Al(111)$ and NiAl(110) for the three different surface terminations. All energies are relative to CO in the gas phase. The CO molecule preferentially adsorbs at sites with maximum Ni and minimum Al. This yields a structure where the Ni atoms involved in CO adsorption have Al as nearest neighbors.

2.2. Structures

It is well known that both Ni_3Al and NiAl are very stable alloys with a high heat of formation [45–47]. γ′-Ni_3Al crystallises in the Cu_3Au $L1_2$ structure (fcc) and β-NiAl in the CsCl B2 structure (bcc). The γ′-Ni_3Al and β-NiAl surfaces are modeled by the close-packed fcc(111) and bcc(110) surfaces respectively. The $Ni_3Al(111)$ and NiAl(110) surfaces are shown in Fig. 1, in which the employed unit cells are also indicated. The lattice constants are calculated to be 3.59 Å for γ′-Ni_3Al and 2.90 Å for β-NiAl respectively. In comparison, the experimental values are 3.57 Å for γ′-Ni_3Al [45,46] and 2.89 Å for β-NiAl [47]. The heats of formation are calculated to be −40.9 kJ/mol for Ni_3Al and −62.6 kJ/mol for NiAl, respectively. This is in good agreement with recent calculations by Wang et al. [48] which gave −41.1 kJ/mol and −62.7 kJ/mol, respectively. The experimental references in the work of Wang et al. [48] have measured heat of formation between −37.6 and −47 kJ/mol for γ′-Ni_3Al and −58.8 to −72 kJ/mol for β-NiAl. It can be seen from Fig. 1 that there are two atop sites, two fcc sites, two hcp sites and three bridge sites on $Ni_3Al(111)$, and two atop sites, two three-fold hollow sites and three bridge sites on NiAl(110). We scan all these possible high-symmetry adsorption sites to determine the most stable site for each adsorbate.

2.3. Chemisorption energies and free energies

The adsorption energies calculated by DFT are extrapolated to conditions relevant for metal dusting using a thermochemistry description of the following reactions:

$$CO(g) + {}^* \rightarrow CO^* \tag{1}$$

$$H_2O(g) + {}^* \rightarrow OH^* + \tfrac{1}{2}H_2(g) \tag{2}$$

$$\tfrac{1}{2}H_2(g) + {}^* \rightarrow H^* \tag{3}$$

The symbol * denotes a site on the surface. The CO chemisorption is investigated since it is the source of carbon. An oxidative environment may prevent carbon deposition on the surface and in steam reforming plants the oxidative agent is H_2O. In contrast, H_2 may reduce the surface. We therefore investigate the dissociative chemisorption energies of both H_2O and H_2. The stability of the adsorbates is described by the chemisorption total energies calculated as

$$\Delta E_{CO} = E(\text{Surface} + CO) - E(\text{Surface}) - E(CO), \tag{4}$$

$$\Delta E_{OH} = E(\text{Surface} + OH) + \frac{1}{2}E(H_2) - E(\text{Surface}) - E(H_2O), \tag{5}$$

$$\Delta E_{H} = E(\text{Surface} + H) - E(\text{Surface}) - \frac{1}{2}E(H_2). \tag{6}$$

E is the total DFT energy of the given system (surface with molecule, surface or molecule in the gas phase), and ΔE describes the

Table 3
Summary of the adsorption energies on the different surfaces. The results for Ni(111) are taken from Ref. [11] and presented for comparison. All energies are in eV.

	Bulk termination		Ni-rich		Al-rich		Ni overlayer		Ni
	Ni_3Al	NiAl	Ni_3Al	NiAl	Ni_3Al	NiAl	Ni_3Al	NiAl	
ΔE (CO)	−1.98	−0.85	−1.78	−1.32	−1.42	−0.21	−1.88	−1.56	−1.53
ΔE (C)	0.89	2.71	1.02	1.68	2.12	2.12	0.83	1.21	1.26
ΔE (OH)	−0.21	−0.41	0.15	0.16	−0.39	−0.72	0.14	0.04	0.38
ΔE (H)	−0.70	−0.14	−0.55	−0.41	−0.38	0.15	−0.56	−0.52	−0.35

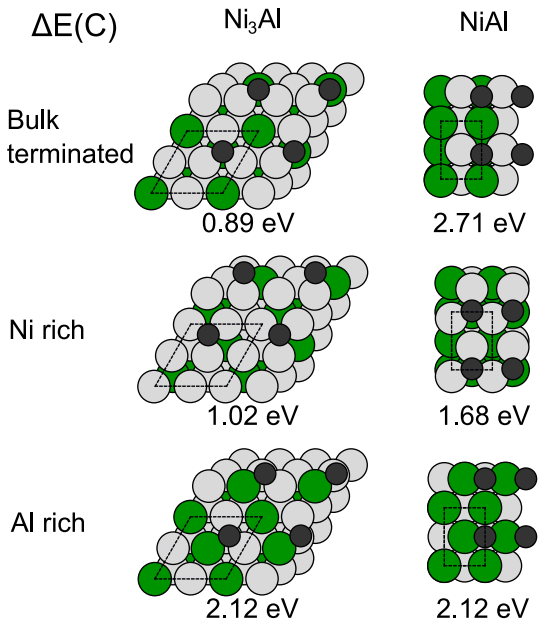

Fig. 4. C adsorption on $Ni_3Al(111)$ and NiAl(110) for the three different surface terminations. All energies are relative to graphite. The C atom preferentially adsorbs at sites with maximum Ni and minimum Al. This yields a structure where the Ni atoms involved in C adsorption have Al as nearest neighbors.

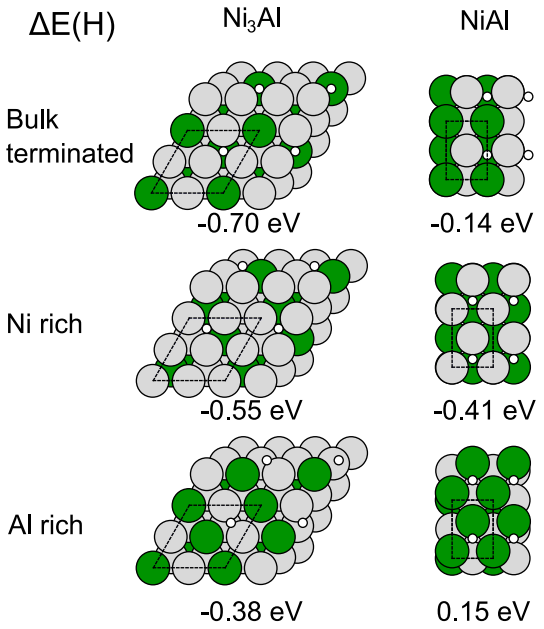

Fig. 6. H adsorption on $Ni_3Al(111)$ and NiAl(110) for the three different surface terminations. All energies are relative to H_2 in the gas phase. The H atom preferentially adsorbs at sites with maximum Ni coordination.

stability of the adsorbate to the surface. The free energies of adsorption for CO, OH or H_2 are given by the following equations

$$\gamma_{CO} = G(\text{Surface} + N\cdot\text{CO}) - G(\text{Surface}) - N\cdot\mu_{CO}, \quad (7)$$

$$\gamma_{OH} = G(\text{Surface} + N\cdot\text{OH}) - G(\text{Surface}) - N\cdot\mu_{H2O} + N\cdot\tfrac{1}{2}\mu_{H2}, \quad (8)$$

$$\gamma_{H} = G(\text{Surface} + N\cdot\text{H}) - G(\text{Surface}) - N\cdot\tfrac{1}{2}\mu_{H2}. \quad (9)$$

Here, $G(\text{Surface} + N\cdot X)$ is the Gibbs free energy of the surface with species X adsorbed, N is the number of adsorbed molecules, and μ_X is the chemical potential of the respective species X in the gas phase. The clean surface is chosen as the zero point. We approximate the free energy of the surface without adsorbates with the DFT energy. We neglect the enthalpy and entropy contributions arising from the vibrations of the adsorbates on the surface. This implies that:

$$G(\text{Surface} + N\cdot X) \approx E_{DFT}(\text{Surface} + N\cdot X) + E_{ZPE}(\text{Surface} + N\cdot X). \quad (10)$$

Here, E_{DFT} is the calculated DFT energy and E_{ZPE} is the zero point energy of the species X on the surface. The zero-point energy is assumed constant for all surfaces and is adapted from Jones et al. [49].

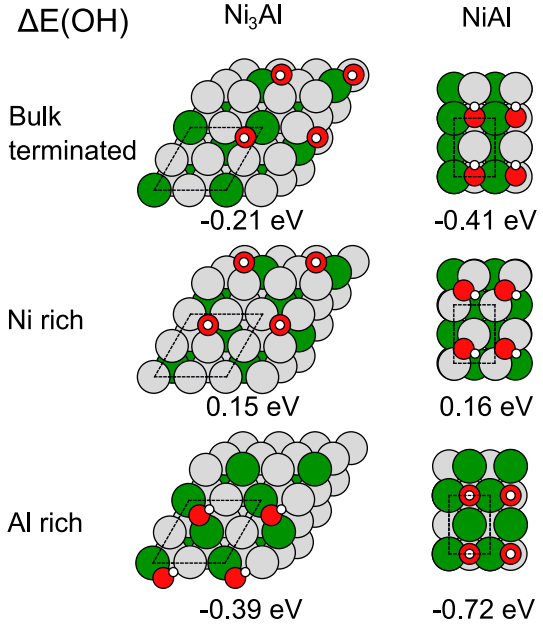

Fig. 5. OH adsorption on $Ni_3Al(111)$ and NiAl(110) for the three different surface terminations. All energies are relative to H_2O and H_2 in the gas phase. The OH molecule preferentially adsorbs at sites which highest possible Al coordination.

2.4. Ranges of chemical potentials for gas phase species

The chemical potential of the species X in the gas-phase at temperature T and pressure p, relative to the vacuum level is given by

$$\mu_X^{T,p} = E_{ZPE} + \Delta_f H_X^{0-T} - TS_X^T + k_B T \ln\left(\frac{p(X)}{p^0}\right). \quad (11)$$

E_{ZPE} is the zero-point energy, which is a function of the vibrational frequencies, ν_i, and is given by

$$E_{ZPE} = \sum_i \frac{h\nu_i}{2} \quad (12)$$

Here, h is Planck's constant. The enthalpy change, from 0 K to a finite temperature T, is given by $\Delta_f H_X^{0-T}$ and the entropy at temperature T is given by S_X^T, k_B is Boltzmann's constant and p^0 is the standard pressure (1 bar). The enthalpy and entropy values as well as the vibrational frequencies are taken from standard thermodynamic databases [50]. The zero of the chemical potentials is taken to be at standard conditions, i.e., room temperature and a pressure of 1 bar. The reference level is changed from vacuum level to standard condition by

$$\Delta\mu_X = \mu_X^{T,p} - \mu_X^0. \quad (13)$$

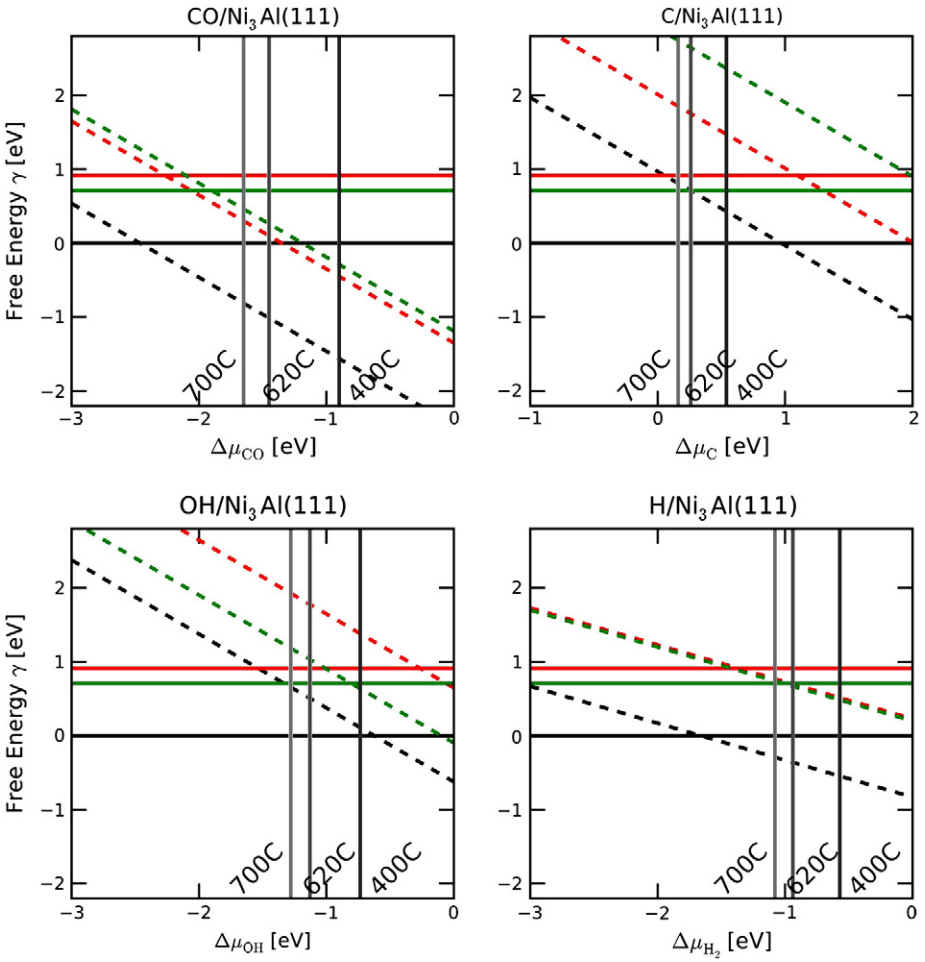

Fig. 7. Free energy diagrams for CO, C, OH and H adsorption on $Ni_3Al(111)$. Energies are according to the free energy reactions 1–3. The black lines are for the bulk termination, red lines for the Ni-rich termination and green lines for the Al-rich termination. Solid lines are the surfaces without adsorbates and dashed lines surfaces with adsorbates. The vertical lines indicate the chemical potentials for each of the species in the gas phase adapted from Ref. [19]. The composition is 25% CO, 73% H_2 and 2% H_2O at the temperatures $T = 400$, 620, and 700 °C.

In the above equation, $\mu_X^{T,p}$ is given in Eq. (11), and μ_X^0 is the chemical potential at standard condition taken from standard tables [51] and listed in Table 1. The quantity $\Delta\mu_X$ indicates how far away the considered reaction conditions are from standard conditions and is listed in Table 2. The OH chemical potential range and values are determined by

$$\Delta\mu_{OH} = \Delta\mu_{H2O} - \tfrac{1}{2}\Delta\mu_{H2}. \quad (14)$$

The reference state for carbon is chosen to be graphite, and not CO. This gives a more convenient relation to the carbon activity, a key parameter in the field of metal dusting corrosion [2]. In the following, it is demonstrated, how the free energy of adsorbed carbon is calculated, and how the chemical potential of carbon in a gas environment relative to the chemical potential of carbon in graphite influences this. The stability of carbon on the surface is set relative to carbon in graphite, since this tells us whether the thermodynamics favors the formation of graphite. The adsorption free energy for carbon adsorption is calculated as follows:

$$\begin{aligned}\gamma &= G(\text{Surface} + \text{C}) - G(\text{Surface}) - N\cdot\mu_C \\ &\approx E(\text{Surface} + \text{C}) - E(\text{Surface}) - N\cdot\mu_C.\end{aligned} \quad (15)$$

The carbon chemical potential μ_C is determined by the carbon source, which may be a gas or carbon dissolved in the bulk. In a steam-reforming or metal-dusting environment, there are three carbon-forming reactions [1,2]:

$$CH_4 \rightarrow C + 2H_2 \quad \text{Methane decomposition} \quad (16)$$

$$CO + H_2 \rightarrow C + H_2O \quad \text{CO reduction reaction} \quad (17)$$

$$2CO \rightarrow C + CO_2 \quad \text{Boudouard reaction} \quad (18)$$

We calculate μ_C from the CO reduction reaction since it is kinetically more favorable than the Boudouard reaction [2,3]. At the conditions considered, thermal cracking of methane is not relevant. The carbon chemical potential is then

$$\mu_C = \mu_{CO} + \mu_{H2} - \mu_{H2O}. \quad (19)$$

We relate μ_C to the graphite by introducing the quantity $\Delta\mu_C$

$$\Delta\mu_C = -\Delta G = \mu_C - \mu_{C,\text{graphite}}. \quad (20)$$

Here, μ_C is the chemical potential of carbon in the gas-phase and $\mu_{C,\text{graphite}}$ is the DFT energy per carbon atom in graphite, set relative to standard conditions according to Eq. (13).

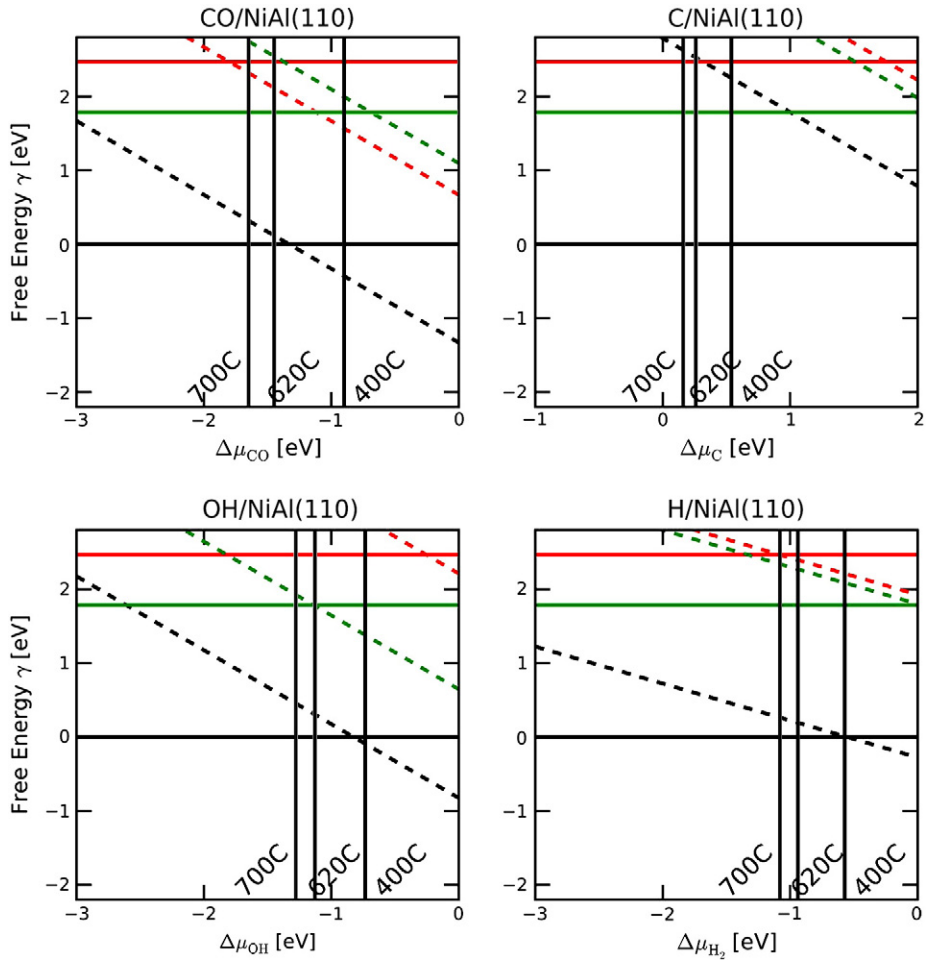

Fig. 8. Free energy diagrams for CO, C, OH and H adsorption on NiAl(110). Energies are according to the free energy reactions 1–3. The black lines are for the bulk termination, red lines for the Ni-rich termination and green lines for the Al-rich termination. Solid lines are the surfaces without adsorbates and dashed lines surfaces with adsorbates. The vertical lines indicate the chemical potentials for each of the species in the gas phase adapted from Ref. [19]. The composition is 25% CO, 73% H_2 and 2% H_2O at the temperatures $T = 400$, 620, and 700 °C.

In this definition, $\Delta\mu_C > 0$ yields a thermodynamic driving force for graphite formation. The carbon activity of a synthesis gas can then be written as

$$a_c = K\frac{p(CO)p(H_2)}{p(H_2O)}. \quad (21)$$

in which K is the equilibrium constant for the CO reduction reaction. The carbon activity can be related to the carbon chemical potential $\Delta\mu_C$ as

$$\Delta\mu_C = k_B T\, ln a_C. \quad (22)$$

Metal dusting generally occurs at $a_c > 1$ corresponding to $\Delta\mu_C > 0$ [2]. This allows for a simple identification of the metal dusting region in the plots of the carbon adsorption free energy versus the carbon chemical potential. Carbon activities and chemical potentials for relevant experimental conditions have been calculated and are listed in Table 2. The ranges of chemical potential calculated previously [16] are for $\Delta\mu_{CO}$, $\Delta\mu_{H2}$, and $\Delta\mu_{H2O}$ from 0.00 eV to 3.00 eV. All chemical potentials are calculated relative to the standard chemical potential μ_X^0.

3. Results and discussion

3.1. Segregation and surface termination

The gas atmosphere surrounding a metal surface may have an impact on surface stoichiometry, as shown for instance in our previous study of the Ni_3Sn alloy surfaces [16]. Therefore, the first step of this investigation is to study the stability of the different surface terminations for both surfaces, γ′-$Ni_3Al(111)$ and β-NiAl(110), relative to the bulk terminated surfaces, as we need to establish the different surface terminations without adsorbates as a reference. The considered surfaces are (see Fig. 2) the bulk terminated one, a Ni-rich termination, in which the Al atoms in the first layer are exchanged with Ni atoms from the second layer, and an Al-rich termination, in which Ni atoms from the first layer are exchanged with Al atoms from the second layer. The energies are referenced to the bulk terminated surfaces to directly reflect segregation energies. For Ni_3Al, the Ni-rich and Al-rich phases are unstable by 0.95 eV and 0.74 eV per unit cell respectively. These segregation energies may well be compensated by correspondingly high changes in adsorption energy of the adsorbates, so we have to consider adsorbate induced segregation. For NiAl, the Ni-rich and Al-rich phases are unstable by 2.74 eV and 1.78 eV per unit cell respectively. Compared to the Ni_3Al surface, it seems more unlikely that changes in adsorption energies on NiAl can compensate for the segregation energies and render adsorbate

induced segregation possible, but this possibility is investigated nonetheless.

In the following, the results for the adsorption of CO, C, OH, and H on the different surface terminations are presented and discussed. We also investigate a Ni overlayer, which may form on the surface upon Al consumption by oxidation. All adsorption energies are summarised in Table 3, which also contains previous results for Ni(111) for comparison. Subsequently, the adsorption energies are extrapolated to metal dusting conditions via the chemical potential formalism, as described in Sections 3.3 and 3.4. This allows establishing, under which conditions the surfaces will be covered by carbon-containing species and under which conditions they will be hydroxylated.

3.2. Adsorption of CO

The chemisorption energies of CO on the six different surfaces have been calculated and the most stable geometries and corresponding adsorption energies are shown in Fig. 3. It is seen that CO is most stable on the bulk terminated surfaces on $Ni_3Al(111)$ and the Ni-rich termination on NiAl(110). CO adsorbs much stronger on all $Ni_3Al(111)$ surfaces than on the NiAl(110) surfaces. In general, CO tries to maximise the number of Ni neighbors and minimise the number of Al neighbors. As CO can coordinate to more Ni atoms on the Ni_3Al surface, the binding on this surface is much stronger. The most stable geometry yields a binding energy of −1.98 eV on $Ni_3Al(111)$. This is comparable to Ni(111), which adsorbs CO with −1.53 eV and on $Ni_3Sn(0001)$ with −1.77 eV. One can discern the same stabilising effect for CO binding on Ni_3Al as for Ni_3Sn, namely that both Al and Sn as a second-nearest neighbor strengthen CO adsorption to the Ni. For NiAl(110) it is noticeable that CO is most stable on the Ni-rich surface. The reason for this is, that Ni in the topmost layer is stretched relative to a bulk Ni lattice constant resulting in a stronger binding [52–54]. In all cases, Ni adsorbs in a three-fold hollow site, except for the NiAl(110) bulk terminated surface, on which it adsorbs atop. The overall conclusion is that compared to Ni(111), CO adsorption is stabilised on $Ni_3Al(111)$ and weakened on NiAl(110).

3.3. Adsorption of C

The adsorption energies of carbon are calculated relative to graphite, even though carbon is deposited on the surface from CO (Table 3). This choice enables us to predict the thermodynamical driving force for graphite formation on the surface. Structures and energies are depicted in Fig. 4. The overall trend for C adsorption is the same as for CO. The most stable site for $Ni_3Al(111)$ is the threefold hollow site on the bulk terminated surface, for which the adsorption energy is 0.89 eV. However, adsorption on this termination is only slightly more stable than on the Ni-rich termination. Adsorption on both terminations corresponds to a stabilisation of C adsorption compared to Ni(111), for which the adsorption energy is 1.26 eV. In contrast, C on NiAl(110) adsorbs strongest on the Ni-rich termination in a three-fold site, with an adsorption energy of 1.68 eV. This means that C is destabilised on NiAl(110) compared to Ni(111). In general, the trends for C adsorption are very similar to CO adsorption. This is not surprising, as both C and CO favor coordination to Ni heavily over coordination to Al.

3.4. Adsorption of OH

The adsorption energy of OH is calculated relative to H_2O and H_2 and all structures and energies are shown in Fig. 5. In general, the adsorption geometries of OH are different than the ones of CO and C, since OH preferentially adsorbs on a bridge site coordinating to Al in the surface layer. The overall result is that O significantly prefers coordination to Al over coordination to Ni and binds to Al wherever possible. Thus, for both surfaces, the Al-rich terminations lead to the most stable adsorption, and the Ni-rich surfaces to the least stable adsorption. However, on the Ni-rich Ni_3Al there are no Al atoms in the top layer and thus OH adsorbs in an fcc site, the same as on Ni(111) (see Fig. 5). Likewise, on the Ni-rich NiAl(110) surface, there are no Al atoms in the top layer, but here OH adsorbs on a bridge site. Compared to Ni(111), OH adsorption is stabilised on both NiAl(110) and $Ni_3Al(111)$ surfaces, but more significantly on the NiAl(110) surface. This can be easily understood, as the Al-rich termination of the NiAl(110) surface corresponds to a full top layer of Al.

3.5. Adsorption of H

The adsorption geometries for H are similar to CO, and the stability of H on the different surfaces has the same ranking as the one for CO and C (see Fig. 6). The results can again be rationalised with the preference of H to coordinate to Ni instead of Al. For Ni_3Al, the most stable site for H adsorption is a hcp site on the bulk terminated surface. At this site, Ni adsorbs with 0.35 eV higher adsorption energy than on Ni(111). On NiAl(110), the preferred adsorption site is a hollow site on the Ni-rich NiAl(110), but here the stabilisation is only 0.06 eV compared to Ni(111).

3.6. Thermochemistry of adsorption

The next step in the analysis is to extrapolate our calculated adsorption energies to metal dusting conditions. For this purpose, we construct free energy diagrams for the adsorption of CO, C, OH and H at chemical potentials corresponding to a gas-composition of 25% CO, 73% H_2 and 2% H_2O [19] at standard pressure (1 bar) and in the temperature range of 700–1100 K. These conditions have previously proven to give rise to metal dusting [19]. The free energy diagrams are shown in Fig. 7 for the $Ni_3Al(111)$ surface and in Fig. 8 for the NiAl(110) surface.

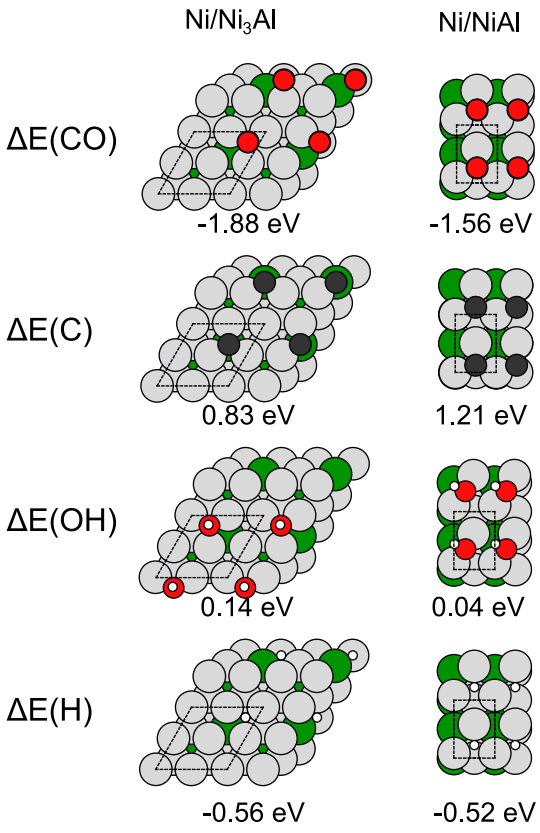

Fig. 9. CO, C, OH and H adsorption on $Ni_3Al(111)$ and NiAl(110) with Ni overlayers.

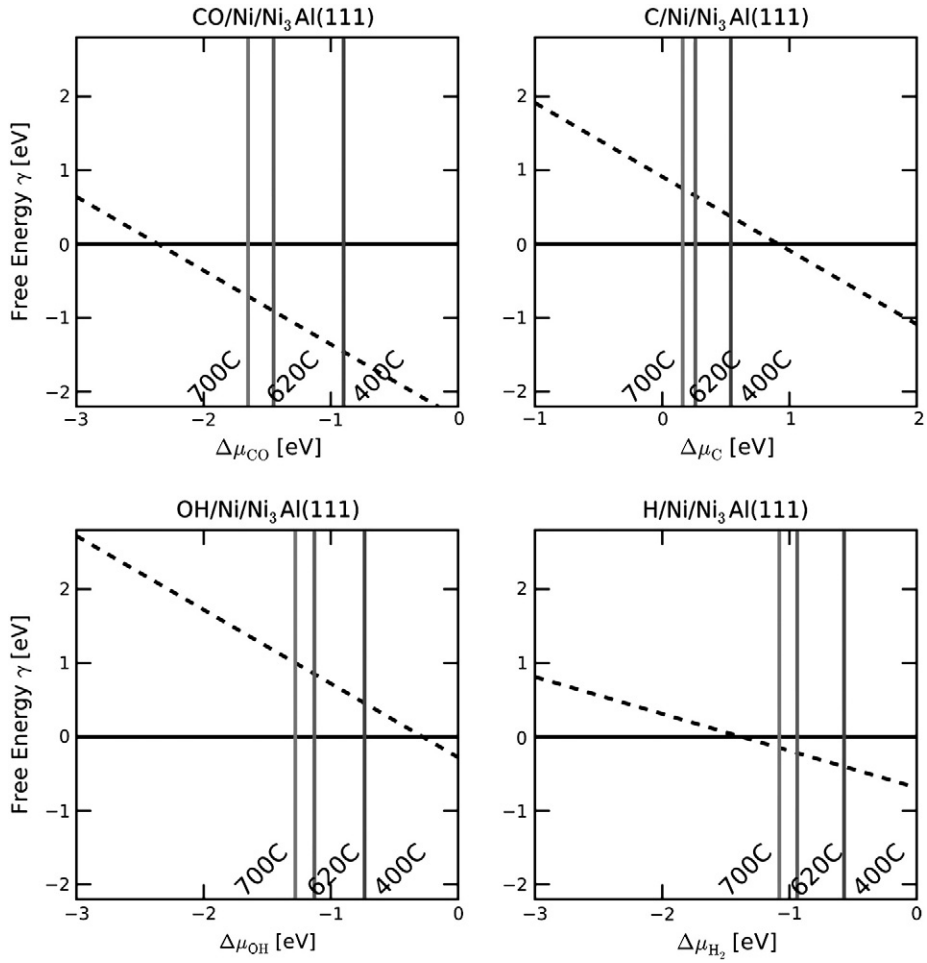

Fig. 10. Free energy diagrams for CO, C, OH and H adsorption on Ni/Ni_3Al(111). The solid line denotes the free energy for a clean Ni overlayer and the dashed line the free energy for the Ni overlayer with adsorbates.

The results for Ni_3Al(111) in Fig. 7 show that the most abundant surface species is CO, but also H and OH are expected to be present to some extent. This can be directly read off the free energy plots in Fig. 7, as the curve with the lowest free energy at a given temperature indicates the species present on the surface. It is clear that none of the adsorbates can induce segregation and hence stabilise the Ni-rich or the Al-rich termination instead of the favored bulk termination. This is because the differences in adsorption energies for the different terminations are smaller than the energies required for segregation. Thus, we predict that on the close-packed surfaces the stoichiometry will not be altered due to adsorbates. It is important to note that the carbonaceous species change the stability order of the segregated surface. While the Al-rich surface is more stable than the Ni-rich surface in the absence of adsorbates, C and CO reverse this order, as they stabilise Ni on the surface compared to Al. However, this stabilisation of Ni is not enough to render Ni segregation to the surface energetically favorable.

Thus we can conclude that any changes in stoichiometry are most likely caused by aluminum consumption for regeneration of the oxide layer or other effects. However, we note that for defects such as phase boundaries, segregation energies may be lower so that stoichiometry variations can be expected there. Here, a mixed γ–γ′ Ni(Al)-Ni_3Al phase has been observed [23].

The results for NiAl(110) are presented in Fig. 8. Also on this surface, CO is the most abundant adsorbate, even though it is closely followed by OH and H. Compared to the Ni_3Al surface, CO adsorption is destabilised whereas OH adsorption is approximately the same, which is why we expect both adsorbates to be present on the surface. For all adsorbates, the stoichiometric termination is clearly the most stable one and the energy difference between the bulk terminated surface and the segregated surfaces is also much larger than for the Ni_3Al(111) surface. This means that on the (110) surface, none of the adsorbates can induce segregation.

Again, we interpret this result such that there must be other driving forces for Ni to segregate to the surface, as observed experimentally [23]. One possibility is that steps and defects are required to allow alteration of the surface stoichiometry. Another possibility is that changes in the surface stoichiometry are caused by Al removal in the top layer to re-form spalled oxide layer. This would correspond to formation of a Ni overlayer on a Ni_3Al or NiAl substrate. These systems are investigated in the following section.

3.7. Ni overlayer — adsorption and thermochemistry

To model the Ni surplus after removal of Al from the surface by oxidation, we consider a Ni overlayer by substituting Al atoms in the top layer with Ni. The adsorption results are shown in Table 3 and Fig. 9. The Ni_3Al(111) with Ni overlayer is termed Ni/Ni_3Al(111). The adsorption geometries and energies for Ni/Ni_3Al(111) are almost identical to those for the Ni-rich termination of Ni_3Al. Compared to Ni(111), adsorption energies for all adsorbates increase, which can also be seen in Table 3 and the free energy diagram in Fig. 10. In practice, this would mean that once Al at the surface is consumed, one is left with a rather reactive surface towards carbon adsorbates and that the presence of OH cannot induce segregation of more Al to this

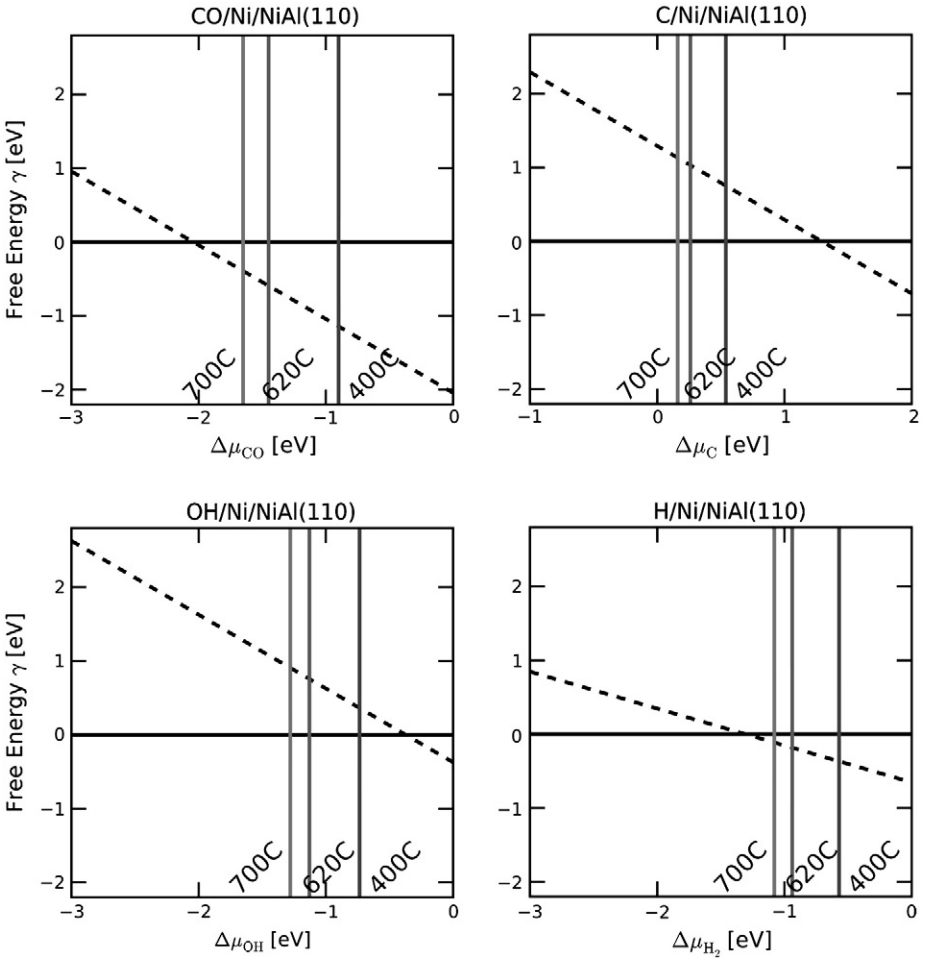

Fig. 11. Free energy diagrams for CO, C, H and OH adsorption on Ni/NiAl(110). The solid line denotes the free energy for a clean Ni overlayer and the dashed line the free energy for the Ni overlayer with adsorbates.

surface. This explains why Ni_3Al is quite vulnerable towards metal dusting at the places, where the Al_2O_3 coating spalls off.

Next, we investigate the Ni/NiAl(110) system shown in Fig. 9, Table 3 and Fig. 11. In this overlayer, the Ni–Ni distances are increased compared to Ni(111) resulting in a more open and reactive surface which binds CO as strong as Ni(111) and stronger than all other investigated NiAl surfaces. These results show that also on NiAl, if the oxide layer spalls off, one is left with a surface which is quite reactive towards carbon-containing adsorbates.

3.8. Discussion

The next step is to combine all obtained results and construct phase diagrams, in which the surface termination and adsorbate with the lowest free energy, as identified in Figs. 7–11, are shown as functions of $\Delta\mu_{OH}$ and $\Delta\mu_{CO}$ for the five different investigated surfaces (Fig. 12). The most relevant aspect for the challenge we investigate is the thermodynamical preference for oxidation or graphite formation, which indicates whether the surface is susceptible to metal dusting or protected by the onset of an oxide layer.

Fig. 12 shows the preferential adsorbate on the surfaces as a function of $\Delta\mu_{OH}$ and $\Delta\mu_{CO}$. Each diagram contains three different areas dictated by the operation conditions. The three areas are the clean surface indicated by * and the most stable surfaces with adsorbates being predominantly CO and OH, indicated by either CO* or OH*. The interesting parameter is the relative size of the areas on the six systems studied. A relatively large area provides a greater span of chemical potential and thereby more flexible operating conditions with a similar resulting surface termination. From the phase diagrams it is clear that the β-NiAl phase is the one that provides the surface most flexible to operating conditions. OH adsorption is sustained on β-NiAl and therefore the surface that is most easily oxidised. Also, the β-NiAl phase has the smallest area in which CO adsorption is favorable and can therefore be expected to be the most metal dusting resistant of all surfaces investigated. In contrast, Ni(111) has a large area for CO adsorption and no preference for OH adsorption under relevant metal dusting chemical potentials. The $Ni_3Al(111)$ surfaces and the $Ni/Ni_3Al(111)$ and Ni/NiAl(110) overlayer surfaces fall in between the two extremes.

The S/C ratio is inversely correlated to the ratio $\Delta\mu_{OH}/\Delta\mu_{CO}$. While a small S/C ratio corresponds to high carbon activities and an aggressive gas, this is reflected in a large positive value for $\Delta\mu_{OH}/\Delta\mu_{CO}$. In contrast, a less aggressive gas is characterised by a high S/C ratio and a small positive value for $\Delta\mu_{OH}/\Delta\mu_{CO}$. Therefore, when the aim is to use as low S/C ratios as possible and still avoid carbon deposition, NiAl offers the most flexible operating conditions due to the larger extend of the OH* area in the phase diagram. It can be seen that the NiAl phase can go as high as $\Delta\mu_{OH}/\Delta\mu_{CO}$ ~0.5, significantly larger than the second ranking Ni_3Al for which the limit is $\Delta\mu_{OH}/\Delta\mu_{CO}$ ~0.05. It should be emphasised that the provided phase diagrams only include the thermodynamic ratio between OH* and CO* on the surface, which are the precursors for forming graphite or oxide at the surface. Thus, our results are in agreement with the previous evidence for NiAl being more protective towards metal dusting than Ni_3Al [23]. However, once Al has been

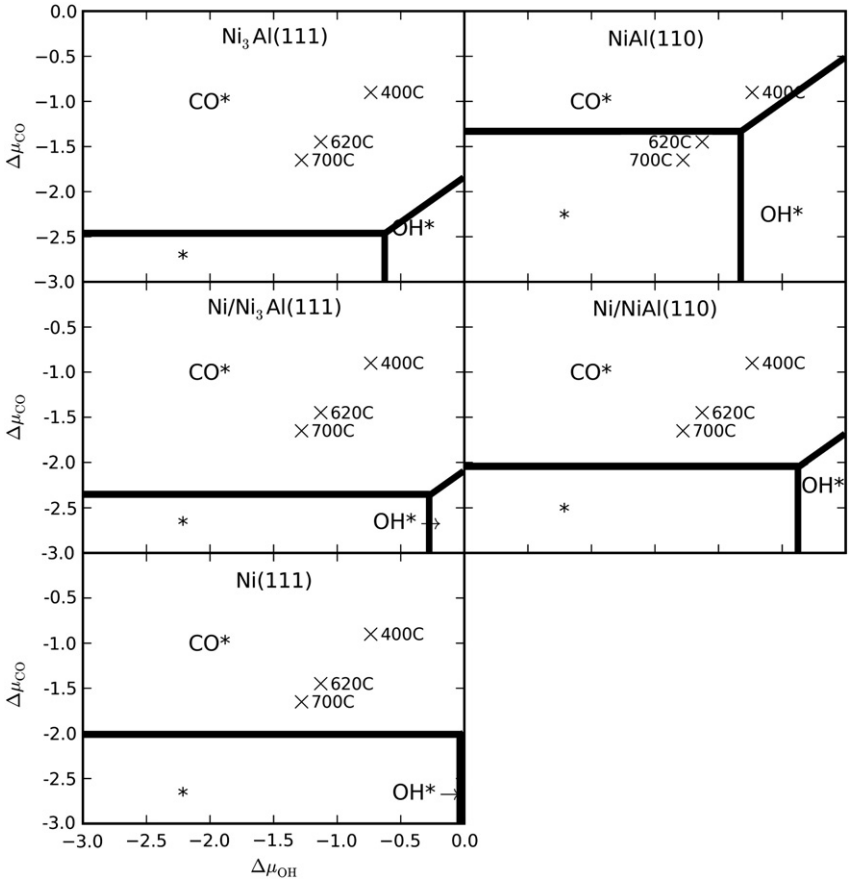

Fig. 12. Phase diagrams for $Ni_3Al(111)$, NiAl(110), $Ni/Ni_3Al(111)$, Ni/NiAl(110), and Ni(111) showing the areas in which the clean surface (denoted by *), the surface with adsorbed CO (denoted by CO*) and the surface with adsorbed OH (denoted by OH*) are the most stable ones.

consumed by reoxidation and in case of oxide spallation, one is potentially left with a very vulnerable surface, as is energetically expensive for Al to segregate to the surface.

5. Conclusions

The adsorption of CO, OH, H and C on the $Ni_3Al(111)$ and NiAl(110) surfaces in the bulk-terminated as well as adsorbate-induced segregated states has been investigated. CO, C, OH and H have different adsorption energies on the different terminations, with carbon and hydrogen exhibiting a clear preference for coordination to Ni, and oxygen a preference for coordination to Al. However, the differences in adsorption energies are not enough to stabilise the segregated states, and thus the bulk-terminated surfaces remain the most stable ones under all relevant metal dusting conditions taken from Ref. [19]. Also, the effect of a Ni overlayer on adsorption was investigated. Ni overlayers on $Ni_3Al(111)$ resemble Ni(111) due to a similar lattice constant. The Ni overlayer on NiAl(110) is more reactive than Ni(111) due to the open structure of the bcc phase. Phase diagrams based on thermochemical calculations showed that NiAl surface provides the largest operating window that allows adsorbed OH. This surface is therefore the one on which an oxide scale can grow at the lowest S/C ratio. The presented results agree well with the work of Young and co-workers [23], as they observed metal dusting on both γ–γ'-Ni_3Al and β-NiAl. The highest metal dusting rate was observed on γ'-Ni_3Al.

Acknowledgements

Souheil Saadi acknowledges financial support from The Danish Agency for Science, Technology and Innovation through the Industrial PhD Fellowship Program. Frank Abild-Pedersen acknowledges financial support from CASE (Catalysis for Sustainable Energy). The DFT calculations were performed with support from the Danish Center for Scientific Computing through grant HDW-0107-07. The authors wish to acknowledge additional support from the Danish Research Agency through grant 26-04-0047. The Center for Atomic-scale Materials Design is sponsored by the Lundbeck Foundation.

References

[1] J.R. Rostrup-Nielsen, J. Sehested, J.K. Nørskov, Adv. Catal. 47 (2002) 65.
[2] H.J. Grabke, Mater. Corros. 54 (2003) 736.
[3] J.R. Rostrup-Nielsen, Catalytic Steam Reforming, Catalysis — Science and Technology, 5, Springer-Verlag, Berlin, 1984.
[4] N.M. Galea, D. Knapp, T. Ziegler, J. Catal. 247 (2003) 20.
[5] Z. Zeng, K. Natesan, Solid State Ionics 167 (2004) 9.
[6] C.M. Chun, T.A. Ramanarayanan, J.D. Mumford, Mater. Corros. 50 (1999) 634.
[7] Z. Zeng, K. Natesan, Chem. Mater. 15 (2003) 782.
[8] Z. Zeng, K. Natesan, Chem. Mater. 17 (2005) 3794.
[9] S. Helveg, C. Lopez-Cartes, J. Sehested, P.L. Hansen, B.S. Clausen, J.R. Rostrup-Nielsen, F. Abild-Pedersen, J.K. Nørskov, Nature 427 (2004) 426.
[10] F. Abild-Pedersen, J.K. Nørskov, J.R. Rostrup-Nielsen, J. Sehested, S. Helveg, Phys. Rev. B 73 (2006) 115419.
[11] S. Saadi, F. Abild-Pedersen, S. Helveg, J. Sehested, B. Hinnemann, C.C. Appel, J.K. Nørskov, J. Phys. Chem. C 114 (2010) 11221.
[12] I. Alstrup, M.T. Tavares, C.A. Bernardo, O. Sørensen, J.R. Rostrup-Nielsen, Mater. Corros. 49 (1998) 367.
[13] J. Zhang, D.M.I. Cole, D.J. Young, Mater. Corros. 56 (2005) 756.
[14] E. Nikolla, A. Holewinski, J. Schwank, S. Linic, J. Am. Cem. Soc. 128 (2006) 11354.
[15] E. Nikolla, A. Holewinski, S. Linic, J. Catal. 250 (2007) 85.
[16] S. Saadi, B. Hinnemann, S. Helveg, C.C. Appel, F. Abild-Pedersen, J.K. Nørskov, Surf. Sci. 603 (2009) 762.
[17] A.M. Molenbroek, J.K. Nørskov, B.S. Clausen, J. Phys. Chem. 105 (2001) 5450.
[18] F. Besenbacher, I. Chorkendorff, B.S. Clausen, B. Hammer, A.M. Molenbroek, J.K. Nørskov, I. Stensgaard, Science 279 (1998) 1913.
[19] C. Rosado, M. Schütze, Mater. Corros. 54 (2003) 831.
[20] S. Strauß, R. Krajak, M. Palm, H.J. Grabke, Mater. Corros. 47 (1996) 701.

[21] W. Brandl, G. Marginean, N. Marginean, V. Chirila, D. Utu, Corros. Sci. 49 (2007) 3765.
[22] H. Liu, W. Chen, Corros. Sci. 49 (2007) 4134.
[23] P. Speck, D.J. Young, J. Zhang, Oxid. Met. 73 (2010) 255.
[24] A.J. Rasmussen, A. Agüero, M. Gutierrez, M.J.L. Østergård, Surf. Coat. Technol. 202 (2008) 1479.
[25] A. Schneider, J. Zhang, Mater. Corros. 54 (2003) 778.
[26] A. Schneider, J. Zhang, G. Inden, J. Corros. Sci. Eng. 6 (2003) H043, Paper.
[27] H. Liu, W. Chen, Mater. Corros. 59 (2008) 311.
[28] K.M. Carling, E.A. Carter, Acta Mater. 55 (2007) 2791.
[29] A. Rabiei A, A.G. Evans, Acta Mater. 48 (2000) 3963.
[30] A.T. Hanbicki, A.P. Baddorf, E.W. Plummer, B. Hammer, M. Scheffler, Surf. Sci. 331 (1995) 811.
[31] A.Y. Lozovoi, A. Alavi, M.W. Finnis, Phys. Rev. Lett. 85 (2000) 610.
[32] G. Kresse, M. Schmid, E. Napetschnig, M. Shishkin, L. Köhler, P. Varga, Science 308 (2005) 1440.
[33] M.V. Bollinger, K.W. Jacobsen, J.K. Nørskov, Phys. Rev. B 67 (2003) 085410.
[34] K. Reuter, B. Scheffler, Phys. Rev. B 65 (2001) 035406.
[35] Available for free at wiki.fysik.dtu.dk/dacapo.
[36] S.R. Bahn, K.W. Jacobsen, Comput. Sci. Eng. 4 (2002) 56.
[37] Available for free at wiki.fysik.dtu.dk/ase.
[38] K. Laasonen, A. Pasquarello, R. Car, C. Lee, D. Vanderbilt, Phys. Rev. B 47 (1993) 10142.
[39] M.C. Payne, M.P. Teter, D.C. Allan, T.A. Arias, J.D. Joannopoulos, Rev. Mod. Phys. 64 (1992) 1045.
[40] D. Vanderbilt, Phys. Rev. B 41 (1990) 7892.
[41] B. Hammer, L.B. Hansen, J.K. Nørskov, Phys. Rev. B 59 (1999) 7413.
[42] H.J. Monkhorst, J.D. Pack, Phys. Rev. B 13 (1976) 5188.
[43] G. Kresse, J. Furthmuller, Comput. Mater. Sci. 6 (1996) 15.
[44] L. Bengtsson, Phys. Rev. B 59 (1999) 12301.
[45] A.J. Bradley, A. Tailor, Philos. Mag. 23 (1937) 1049.
[46] A. Taylor, R.W. Floyd, J. Inst. Met. 81 (1952) 25.
[47] A.J. Bradley, A. Tailor, Proc. R. Soc. London Ser. A 159 (1937) 56.
[48] Y. Wang, Z.K. Liu, L.Q. Chen, Acta Mater. 52 (2004) 2665.
[49] G. Jones, J.G. Jakobsen, S.S. Shim, J. Kleis, M.P. Andersson, J. Rossmeisl, F. Abild-Pedersen, T. Bligaard, S. Helveg, B. Hinnemann, J.R. Rostrup-Nielsen, I. Chorkendorff, J. Sehested, J.K. Nørskov, J. Catal. 259 (2008) 147.
[50] *NIST Standard Reference Database Number 69*, June 2005 Release, http://www.webbook.nist.gov/chemistry/.
[51] *CRC Handbook of Chemistry and Physics*, 88th Edition.
[52] F. Abild-Pedersen, J. Greeley, J.K. Nørskov, Catal. Lett. 105 (2005).
[53] F. Abild-Pedersen, O. Lytken, J. Engbaek, G. Nielsen, I. Chorkendorff, J.K. Nørskov, Surf. Sci. 590 (2005) 127.
[54] M. Mavrikakis, B. Hammer, J.K. Nørskov, Phys. Rev. Lett. 81 (1998) 2919.